AGU PUBLICATIONS

Space Weather

RESEARCH ARTICLE
10.1002/2017SW001671

Key Points:
- Generalized, extensive WEC model simulations provide analogous confidence levels and results as detailed, relatively short simulations
- WSA-ENLIL+Cone model succeeds at predicting fast solar wind radial velocity

Correspondence to:
C. L. Lentz,
christy.lentz@lasp.colorado.edu

Citation:
Lentz, C. L., Baker, D. N., Jaynes, A. N., Dewey, R. M., Lee, C. O., Halekas, J. S., & Brain, D. A. (2018). Statistical Similarities Between WSA-ENLIL+Cone Model and MAVEN in situ Observations from November 2014 to March 2016. *Space Weather*, *16*, 157–171. https://doi.org/10.1002/2017SW001671

Received 28 MAY 2017
Accepted 18 DEC 2017
Accepted article online 26 DEC 2017
Published online 21 FEB 2018

Statistical Similarities Between WSA-ENLIL+Cone Model and MAVEN in Situ Observations From November 2014 to March 2016

C. L. Lentz[1], D. N. Baker[1], A. N. Jaynes[1], R. M. Dewey[2], C. O. Lee[3], J. S. Halekas[4], and D. A. Brain[1]

[1]Laboratory for Atmospheric and Space Physics, University of Colorado Boulder, Boulder, CO, USA, [2]Department of Climate and Space Sciences and Engineering, University of Michigan, Ann Arbor, MI, USA, [3]Space Sciences Laboratory, University of California, Berkeley, CA, USA, [4]Department of Physics and Astronomy, University of Iowa, Iowa City, IO, USA

Abstract Normal solar wind flows and intense solar transient events interact directly with the upper Martian atmosphere due to the absence of an intrinsic global planetary magnetic field. Since the launch of the Mars Atmosphere and Volatile EvolutioN (MAVEN) mission, there are now new means to directly observe solar wind parameters at the planet's orbital location for limited time spans. Due to MAVEN's highly elliptical orbit, in situ measurements cannot be taken while MAVEN is inside Mars' magnetosheath. To model solar wind conditions during these atmospheric and magnetospheric passages, this research project utilized the solar wind forecasting capabilities of the WSA-ENLIL+Cone model. The model was used to simulate solar wind parameters that included magnetic field magnitude, plasma particle density, dynamic pressure, proton temperature, and velocity during a four Carrington rotation-long segment. An additional simulation that lasted 18 Carrington rotations was then conducted. The precision of each simulation was examined for intervals when MAVEN was in the upstream solar wind, that is, with no exospheric or magnetospheric phenomena altering in situ measurements. It was determined that generalized, extensive simulations have comparable prediction capabilities as shorter, more comprehensive simulations. Generally, this study aimed to quantify the loss of detail in long-term simulations and to determine if extended simulations can provide accurate, continuous upstream solar wind conditions when there is a lack of in situ measurements.

Plain Language Summary If we ever have a manned mission to Mars, one of the numerous concerns would be space weather conditions and their effects on spacecraft in flight. One particular element of space weather that we like to focus on is solar wind: plasma that is continuously emitted from the Sun. Solar wind can effect communication between Earth and spacecraft, GPS services, and other vital elements of space travel. We therefore want a good understanding of space weather and want to forecast conditions before ever traveling there. Currently, there are not always means to directly measure solar wind, so we rely on numerical models. In this study, we used the model called WSA-ENLIL+Cone to compare its solar wind measurements and one of our spacecraft orbiting Mars to see how well it did and to see if we can rely on it for solar wind forecasts. As it turns out, the model can be used for forecasting baseline values of different solar wind parameters, for example, temperature, even with limited information. We show in this study that the WSA-ENLIL+Cone model allows us to forecast solar wind conditions and helps us to understand what is going on at that seemingly barren planet.

1. Introduction

With the insertion of Mars Atmosphere and Volatile EvolutioN (MAVEN) into Mars' orbit on 21 September 2014 (Jakosky et al., 2015), new data coming in are being pored over as MAVEN, among other spacecraft, provides first-hand observations of the long-term effects of solar transient events on Mars' atmosphere. MAVEN has an ~ 4.5 h orbit, where it spends at least a few hours in the magnetosheath, and upward of approximately 2 months, when the precessing spacecraft periapsis is at a low solar zenith angle (D. Brain, personal communication, 2017). Attempting to model solar wind conditions during the MAVEN mission, the WSA-ENLIL+Cone model (Arge & Pizzo, 2000; Odstrčil et al., 2002; Xie et al., 2004) was used for the time period of December 2015 to March 2016, along with a separate run that captured solar wind trends from late November 2014

to March of 2016. We report here on the accuracy of the WSA-ENLIL+Cone model's predictions of solar wind parameters such as the interplanetary magnetic field strength, proton density of the plasma, dynamic pressure, proton temperature, and the radial velocity from the two separate runs. We conducted multiple statistical analysis to determine if extended runs are as reliable as relatively short runs. With extensive analysis of the WSA-ENLIL+Cone model's performance, there is a possibility of using the model's predictions for times when MAVEN, or other spacecraft, is unable to obtain in situ measurements during deep-dip campaigns.

Commonly, long-term statistical comparisons tend to lose fine detail for individual events. By requesting an extended, lower resolution simulation that overlapped with a portion of a higher-resolution simulation, we could determine what impacts generalizations had on the performance of the model. Expanding on preexisting performance metrics for solar wind simulations we assessed the model's capacity to provide precise solar wind conditions and to conclude if the extended simulation's results were comparable in accuracy to the detailed run.

2. Background

2.1. The MAVEN Mission

MAVEN is in a highly elliptical orbit with a low-altitude periapsis of ~150 km that allows it to pass through the magnetic pileup boundary and the bow shock (BS) once every orbit, regardless of the boundary altitude changes (see Edberg et al., 2009). MAVEN can therefore measure the solar and solar wind energetic input into the upper atmosphere (e.g., Jakosky et al., 2015) that allows us to explore the interactions of the Sun and the solar wind with the Martian magnetosphere and upper atmosphere. Along with MAVEN there have been multiple other orbiters that can aid in the study of Mars' atmosphere. For example, the Mars Global Surveyor (Acuña et al., 1992) that orbited Mars for 10 years, losing signal in November of 2006, had instruments on board such as a magnetometer (Acuña et al., 1998) but lacked other instruments to observe phenomena such as interplanetary coronal mass ejections (ICME) and solar energetic particles (Falkenberg et al., 2011). Another recent European mission, the Mars Express (Zender et al., 2009), has atmospheric and ionospheric instruments such as the Energetic Neutral Ion analyzer (Barabash et al., 2006) but lacks a magnetometer. For this study, only MAVEN data were used to compare with the WSA-ENLIL+Cone model; however, future work in model validation would benefit from having multiple spacecraft data sets to contrast with. MAVEN includes a set of atmosphere measuring and contextual instruments such as the solar wind electron analyzer (Mitchell et al., 2016), the solar wind ion analyzer (Halekas et al., 2015), the solar energetic particle detector (Larson et al., 2015), and a magnetometer (Connerney et al., 2015). However, as MAVEN ascends or descends into the BS and other layering regions, there are time periods when there is no method to extract data on solar wind parameters such as the velocity of the plasma, particle density, pressure, temperature, and magnetic field properties. This is where solar wind forecasting models can be utilized to predict supplemental solar wind parameter values (e.g., Dewey et al., 2016).

2.2. WSA-ENLIL+Cone Background

Among the numerous space weather models that the Community Coordinated Modeling Center (CCMC) has to offer, the semiempirical Wang-Sheeley-Arge (Arge & Pizzo, 2000; Arge et al., 2004) solar corona model coupled with the three-dimensional magnetohydrodynamic numerical model, ENLIL (ENLIL v2.8f), (Odstrčil, 2003) combined with the Cone model (Millward et al., 2013; Xie et al., 2004) provides descriptions of the propagation of CMEs to specified orbital locations, such as Mars. This combination of models, along with only WSA-ENLIL, has been used in multiple planetary interaction studies such as at Mercury (e.g., Baker et al., 2009, 2011, 2013; Dewey et al., 2015) or at Earth (e.g., Mays et al., 2015).

The WSA model contrives predictions of background solar wind speed and interplanetary magnetic field (IMF) strength out to 21.5 $R_\odot$ from maps of the photospheric magnetic field. The WSA model uses the assumption that far from the Sun, the speed of solar wind depends on the path the wind took as it passed through the lower corona. It follows that if the magnetic flux tube, which guided the flow flares out, had large coronal expansion, then the distant speed is slow. Alternatively, if the magnetic flux tube remained focused (i.e., had small coronal expansion), then the distant speed is fast. The extent of expansion is determined from a current-free extension of the photospheric field (Sheeley Jr. 2017). The WSA uses ground-based observations of the solar surface magnetic field as input to a potential field source surface (PFSS) model (Schatten et al., 1969; Wang & Sheeley, 1992). By applying empirical relationships along with the application of a PFSS magnetic field, the WSA model provides input for ENLIL (Taktakishvili et al., 2009). ENLIL subsequently models

the solar wind flow throughout the heliosphere, assuming equal temperatures and densities for electrons and protons with other microscopic processes being neglected (Odstrčil, 2003). The WSA-ENLIL combination then sets the stage for CMEs to be "injected." To include CME disturbances in the WSA-ENLIL model, this study utilized the Cone model. Initially proposed by Zhao et al. (2002) and further refined by Xie et al. (2004), the Cone model is a simplified representation of CME propagation used to characterize 3-D geometric and kinematic parameters. The model assumes a constant angular diameter of CMEs in the corona that are enclosed by the external magnetic field. Consequently, Cone-modeled CMEs do not expand in latitude in the lower corona, though they can expand in interplanetary space, as described in Odstrčil et al. (2002).

To acquire a WSA-ENLIL+Cone simulation from the CCMC, a list of CME measurements that occurred during the time period of interest must be provided, along with a source for solar magnetograms (e.g., Mount Wilson observatory, Kitt Peak observatory, or Gong observatory). For this study, CME kinematic and geometric properties were gathered from the CCMC Space Weather Database of Notifications, Knowledge, Information (DONKI) database (kauai.ccmc.gsfc.nasa.gov/DONKI). There, approximated Cone-modeled CME properties derived from coronagraphs were used. The database, which contains a catalog of numerous types of solar activity, is a result of the NASA Space Weather Research Center team daily monitoring of the space environment for NASA's science campaigns. DONKI continuously updates a list of derived CME geometries that are obtained from spacecraft that are observing a CME event near the solar limb similar to the process described in Lee et al. (2013). It is noted as a limitation of the database that some CMEs may be missed due to real-time data gaps (see Mays et al., 2015).

The synoptic solar magnetograms chosen for this study were selected from the National Solar Observatory's Global Oscillation Network Group (GONG) (Harvey et al., 1996). GONG's magnetograms were elected due to their hourly cadence. GONG remaps minute-by-minute images to get a weighted sum to form a full-surface map of the photospheric magnetic flux density (gong.nso.edu). However, it is noted on the model run request site that GONG data have known issues with the polar fields, which are being studied by the GONG staff (ccmc.gsfc.nasa.gov).

It should also be mentioned that the WSA-ENLIL+Cone model's CME arrival times are reliant upon the initial CME geometry input parameters (Mays et al., 2015). Accuracy has also been shown by Lee et al. (2013) to be heavily dependent on the initial precision of the modeled background solar wind, which is determined by the inputted solar magnetograms supplied by the GONG observatories. In comparable studies, the most favorable magnetograms are ones that are updated on an hourly cadence to provide the utmost complete global photosphere magnetic field map.

To test the model's validity during the two runs, MAVEN's solar wind ion analyzer and magnetometer were used to determine when MAVEN was in upstream solar wind. The SWIA instrument's absolute solar wind density measurements are subject to uncertainties due to ambiguities in the sensitivity calibration as mentioned in Dewey et al. (2016). When comparing MAVEN's proton temperature values to WSA-ENLIL+Cone estimated temperatures, values derived from SWIA for the orbited averaged data are at times overestimated because temperature is a partial moment of the solar wind plasma distribution. This is especially true for the coldest solar wind because due to instrument resolution, the measured distribution will artificially be broadened (J. Halekas, personal communication, 2017).

For both periods of studies, similar to Dewey et al. (2016), we chose SWIA and MAG data from times when MAVEN was considered to be in upstream solar wind. This is characterized by having no exospheric or magnetospheric events present in the data. These observations were then averaged over each orbit, where several filters were applied to the data to determine intervals of upstream solar wind. These filters consisted of altitude, sonic Mach number, the bulk flow velocity, and the root-mean-square (RMS) magnetic field fluctuations. These filters also enabled us to exclude false positives for upstream conditions, for example, when MAVEN is taking measurements in Mars' magnetosheath and foreshock.

3. Data Observations and Analyses

3.1. Analysis of Detailed Run From December 2015 to March 2016

We compared the results from the WSA-ENLIL+Cone model with direct solar wind and IMF measurements from the MAVEN spacecraft over the period from December 2015 to March 2016. In this period of study, there was a total of 83 CMEs documented on the DONKI database, all of which were "injected" into ENLIL.

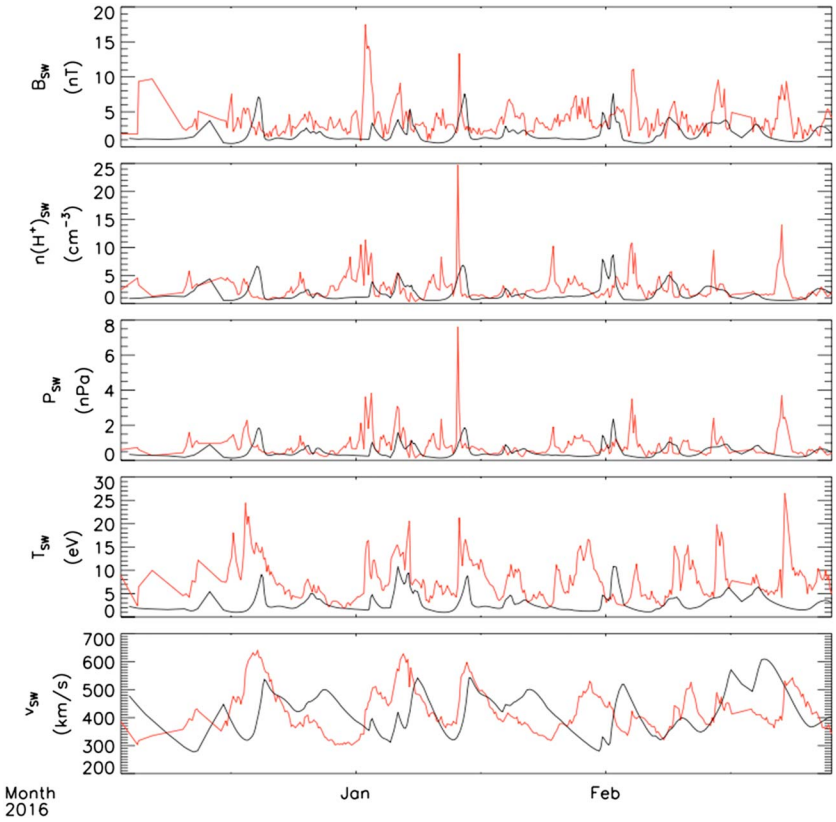

Figure 1. The WSA-ENLIL+Cone (WEC) model results for the detailed period from December 2015 to March 2016. WEC (black) computed values and MAVEN (red) actual observations of (first panel) IMF *B* and solar wind parameters (second panel) *N*, (third panel) *P*, (fourth panel) *T*, and (fifth panel) *V*. Note the sparsity of MAVEN's data at the beginning of this time period is due to MAVEN not being in an interval of pristine solar wind.

Figure 1 shows the modeled results of the detailed run at the Mars location (black) in comparison with the MAVEN in situ measurements (red).

To analyze the accuracy of the detailed WSA-ENLIL+Cone run compared to MAVEN observations, we first identified by how much or how little the modeled distribution underestimates or overestimates each solar wind parameter. To visualize this, Figure 2 includes histograms of the frequency distributions of the detailed run from December 2015 to March 2016. The model's data have been orbit averaged in order to compare to MAVEN's orbit averaged data sets. The bin sizes were chosen specifically for each parameter to adequately

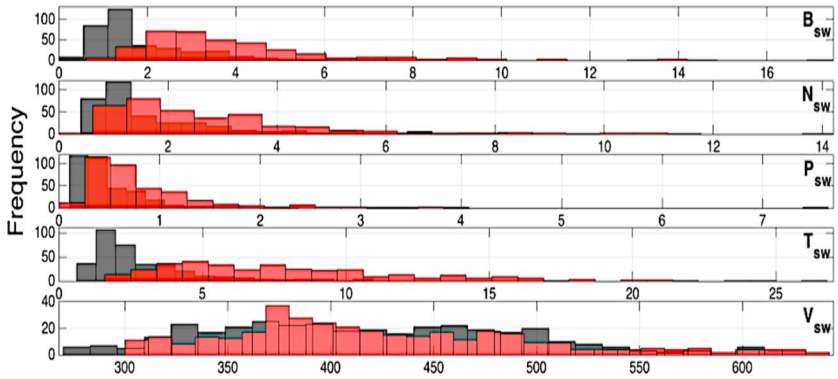

Figure 2. Histograms of frequency distributions from the entire detailed run from December 2015 to March 2016. The model's data (black) have been orbit averaged to compare to MAVEN's orbit-averaged data sets (red). The bin sizes were chosen specifically for each parameter to adequately represent the data density.

Figure 3. Identified CME shock arrival times depicted in light green from the detailed simulation (December 2015 to March 2016). MAVEN's observations are depicted in red, while WSA-ENLIL+Cone data set is in black.

represent the data density. Solar wind speed is one of the best represented parameters. These histograms help to demonstrate the performance of the ENLIL component of WSA-ENLIL+Cone. ENLIL is responsible for the output of the five main solar wind parameters examined in this paper after receiving CME parameter information from the WSA and Cone model. The model's strength in capturing solar wind speed distributions can be noted in Figure 2 (bottom panel). It can also be seen that the mean proton temperature is underpredicted for the time period, as was found by Dewey et al. (2016). It is also clear that the WSA-ENLIL+Cone model

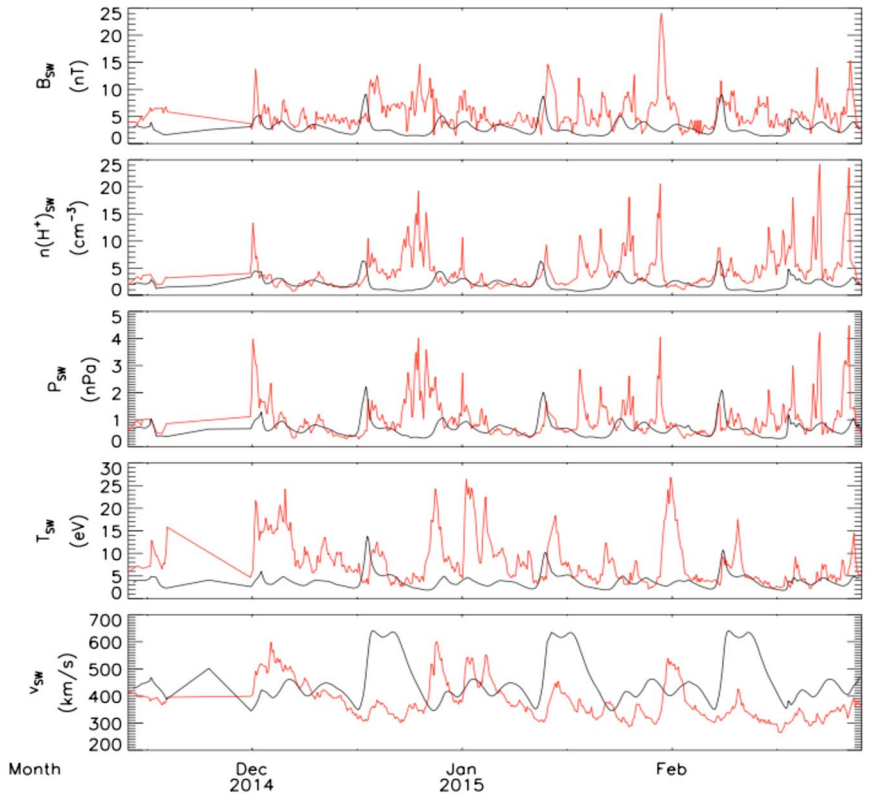

Figure 4. The WEC model results (black) for the extended run from November 2014 to March 2015, along with MAVEN observations (red). The five solar wind parameters in each panel are as follows: magnitude of the IMF (*B*) measured in nanotesla, the number of protons in solar wind (*N*) measured in cm^{-3}, the dynamic pressure (*P*) measured in nPa, the magnitude of temperature (*T*) measured in eV, and radial velocity measured in km/s.

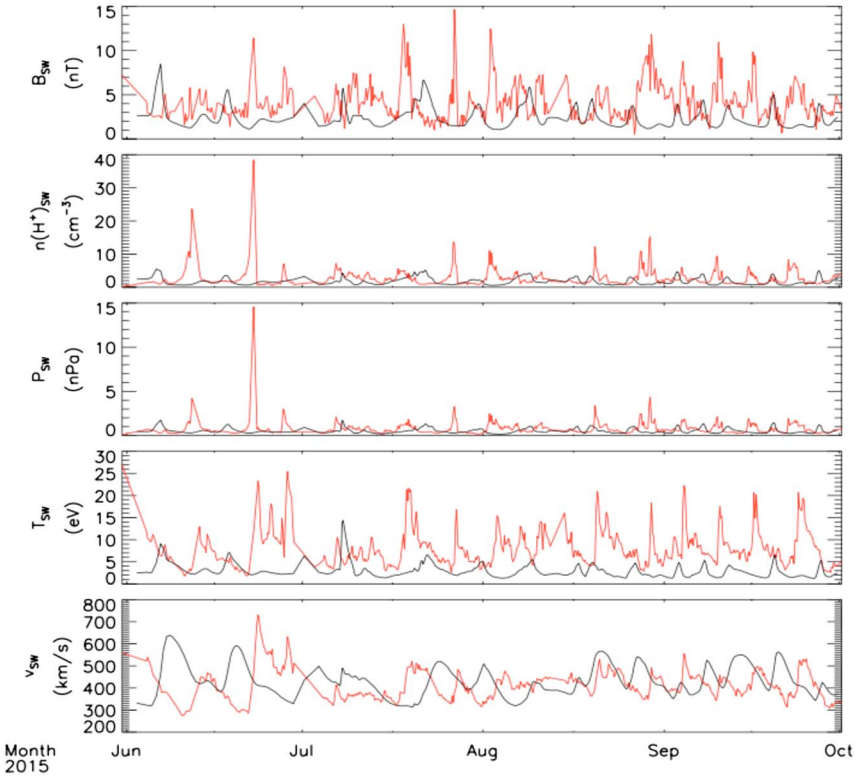

Figure 5. The WEC model results (black) for the extended run from June 2015 to October 2015 along with MAVEN observations (red).

continuously underpredicts IMF strength for CMEs, as stated by Dewey et al. (2015). This can be attributed to the WSA-ENLIL+Cone model not including a magnetic cloud in simulation (see Falkenberg et al., 2011).

To compare how well the model does at recovering solar wind transient features, the CME shock arrival times that MAVEN observed are plotted in Figure 3, along with the modeled and in situ wind parameters. These shock arrival times came from the findings of Lee et al. (2017) where MAVEN-observed solar wind transient and energetic particle events were documented. As defined in Falkenberg et al. (2011) a shock at Mars is a jump in the pressure proxy of at least 2 nPa.

To evaluate the accuracy of shock detection, we compare the peak dynamic pressure between WSA-ENLIL+Cone and MAVEN. For this time period, the first CME that impacted Mars was on 2 January 2016/03:50:00 UT. The peak dynamic pressure value was recorded to be 3.4 nPa. The second CME shock arrival time was recorded to be on 6 January 2016/02:40:00 UT measuring 3.0 nPa. The last impacting CME for this time range was on 4 February 2016/06:05:00 UT, and the peak dynamic pressure was recorded at 3.3 nPa.

Referencing the WSA-ENLIL+Cone dynamic pressure data set, the model estimated the dynamic pressure on the 2 January 2016/03:50:00 UT CME to be 0.25 nPa, 6 January 2016/02:40:00 UT at 1.59 nPa, and finally, 4 February 2016/06:05:00 UT at 0.22 nPa. Therefore, the model underestimated the peak dynamic pressure on average throughout this period by a factor of around 10. It should be noted, for this detailed period, that there are many apparent shocks in pressure that are missed by the simulation. The largest shock event, which occurred on 13 January 2016/15:00:00 UT measuring 7.59 nPa by MAVEN, was missed by WSA-ENLIL+Cone. The closest event that the model recorded was on 14 January 2016/12:40:00 UT measuring 1.97 nPa.

3.2. Comparison Between WSA-ENLIL+Cone Model Simulation Results and MAVEN Data for an Extended Time Range

Moving on to the extended simulation, we attempted to determine if this extensive run had an analogous performance to the detailed run. One of the desired insights to gain in this study was to resolve if the extended simulation had loss of detail in any transient disturbances. To determine if the WSA-ENLIL+Cone model could be used to obtain continuous solar wind forcing for an extended period, we requested an extensive simulation

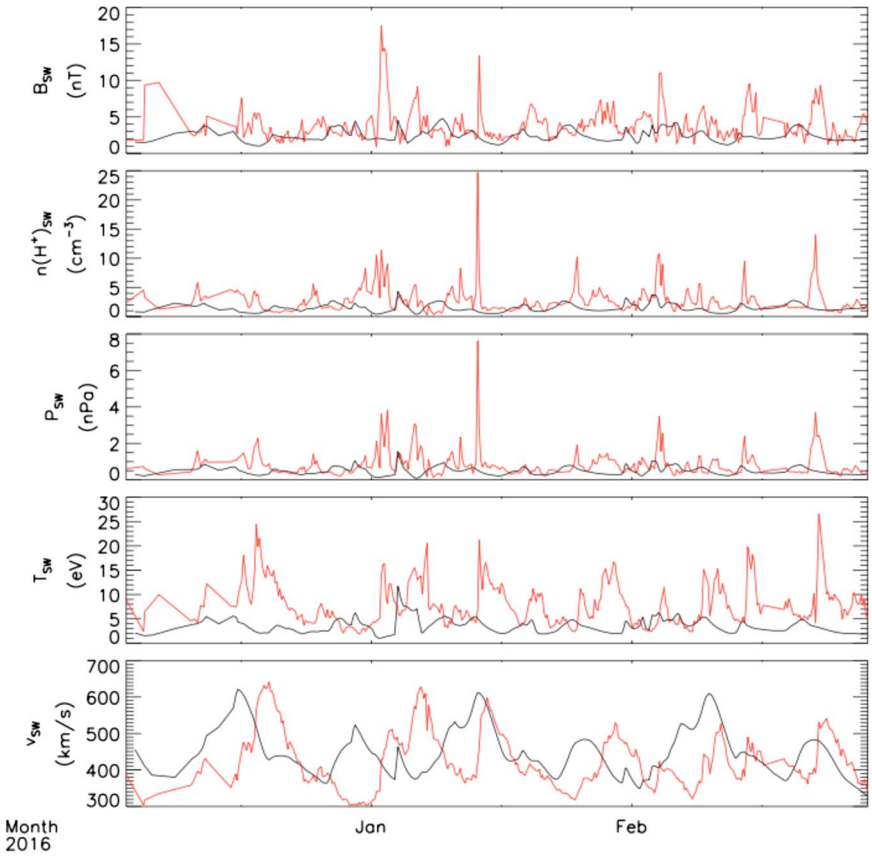

Figure 6. The WEC model results (black) for the extended run from December 2015 to March 2016. December 2015 to March 2016 season plotted for extended run, along with MAVEN observations (red).

from November 2014 to March 2016. The simulation of the propagation, evolution, and interaction of solar wind disturbances en route to Mars is a challenging task for such a lengthy stretch of time. The inhomogeneous nature of the flow along with a large spatial domain makes running these simulations computationally expensive. Hence, the extended run had to be broken down into runs. We arbitrarily selected to look at three seasons that composed the simulation for purposes of better visualization. To model the time period from November 2014 to March 2016, the total number of CMEs was filtered. The CMEs that were determined to be too slow or too narrow were excluded from the extended run. For example, CMEs that were detected by the Sun Earth Connection Coronal Heliospheric Investigation (Howard et al., 2008) on board the Solar Terrestrial Relations Observatory (STEREO A/B) (Kaiser et al., 2007) and Large Angle Spectrometric Coronagraph C2 or C3

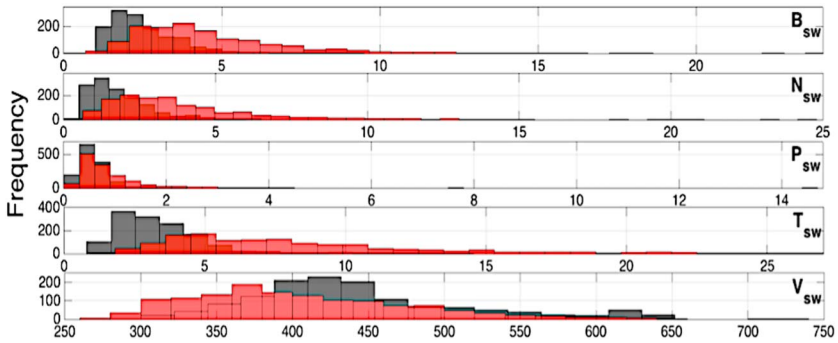

Figure 7. Histograms of frequency distributions from the entire extended run from November 2014 to March 2016, where the model's data (black) have been orbit averaged to compare to MAVEN's orbit-averaged data sets (red). The bin sizes were chosen specifically for each parameter to adequately represent the data density.

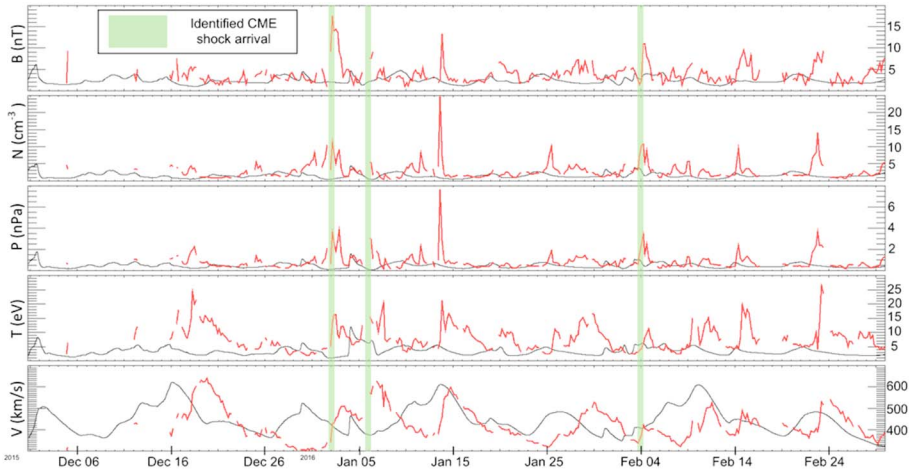

Figure 8. Identified CME shock arrival times (light green) from December 2015 to March 2016 for the extended run as observed by MAVEN (red) and predicted by WSA-ENLIL+Cone (black).

on board Solar and Heliospheric Observatory (Domingo et al., 1995) that were detected to be under 300 km/s were excluded along with CMEs that had a half width less than 10. The total number of CMEs documented on the DONKI website for the first winter season of November 2014 to March 2015 was 197; 101 of which were used in the simulation. For the summer season from June 2015 to October 2015, out of the 179 total CMEs, 92 were used. Finally, for the second winter period, 46 out of the 83 total CMEs were used. The following figures (Figures 4–6) show a broad overview of the data obtained from the WSA-ENLIL+Cone simulation for each of the three seasons.

Continuing with preliminary analyses, we have included another display (Figure 7) of histograms of frequency distributions of the five solar wind parameters from the entire extended period.

As was conducted with the detailed simulation, we report on the shock arrival times as observed by MAVEN for the extended run. The shock arrival times for the extended run were also taken from Lee et al. (2017). The second winter period during the extended run is plotted in Figure 8 with identified shock arrival times at MAVEN's orbital location. The values are determined from the orbit-averaged resolution upstream solar wind data set. During the winter period from December 2015 to March 2016 for the extended run, MAVEN detected a total of three CMEs. The first arriving on 2 January 2016/03:50:00 UT measuring 3.4 nPa, 6 January 2016/02:40:00 UT measuring 3.0 nPa, and then on 4 February 2016/06:05:00 UT measuring 3.3 nPa. The WSA-ENLIL+Cone model's corresponding dynamic pressure values were 0.16 nPa, 0.16 nPa, and 0.87 nPa, respectively. Therefore,

Figure 9. Identified CME shock arrival times (light green) from June to October 2015 for the extended run as observed by MAVEN (red) and predicted by WSA-ENLIL+Cone (black).

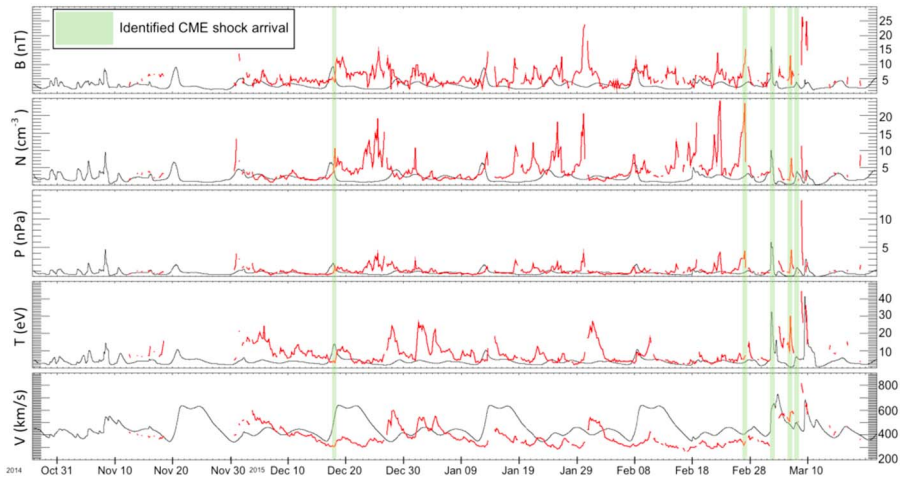

Figure 10. Identified CME shock arrival times (light green) from November 2014 to March 2015 for the extended run as observed by MAVEN (red) and predicted by WSA-ENLIL+Cone (black).

on average, the model underestimated peak dynamic pressure by a factor of ~15 compared to the detailed period where peak dynamic pressure was underpredicted by a factor of ~10.

The June 2015 to October 2015 season is depicted in Figure 9. MAVEN recorded a CME shock arrival on 6 July 2015/20:00:00 measuring 2.1 nPa and a second CME on 6 October 2015/17:30:00 measuring 3.5 nPa. The WSA-ENLIL+Cone model's corresponding measurements during these time periods were 0.53 and 2.05 nPa, respectively, demonstrating an underprediction of peak dynamic pressure by a factor of ~3.

Figure 10 displays the first winter period from November 2014 to March 2015 where a total of five CMEs made impact with Mars. MAVEN observed the first on 18 December 2014/02:00:00 UT measuring 1.6 nPa, 27 February 2015/02:30:00 UT measuring 4.5 nPa, 4 March 2015/04:40:00 measuring 6.5 nPa, 7 March 2015/04:00:00 UT measuring 4.5 nPa, and finally, 8 March 2015/21:00:00 UT measuring 12.5 nPa.

The corresponding simulated model values for these time periods were 1.91 nPa at 18 December 2014/02:00:00 UT, 0.69 nPa at 27 February 2015/02:30 UT, 5.97 nPa at 4 March 2015/04:40:00 UT, 1.38 nPa at 7 March 2015/04:00:00 UT, and 0.88 nPa at 8 March 2015/21:00:00 UT. The WSA-ENLIL+Cone model therefore underpredicted MAVEN-observed peak dynamic pressure values by a factor of 5. Averaging the underestimations throughout the entire extended period of analysis, WSA-ENLIL+Cone underpredicted observations by a factor of 8, compared to the detailed period of analysis that underpredicted the three documented CMEs by a factor of 10.

3.3. Comparison Between WSA-ENLIL+Cone Model Detailed and Extended Simulation

Along with assessing the variability of each data set by examining histograms, we also evaluated various moments of both data sets. Measures of skewness and kurtosis were utilized to characterize the location

Table 1
Skewness for the Five Solar Wind Parameters for the WSA-ENLIL+Cone Model and MAVEN

Parameter	Dec 2015 to Mar 2016 (Detailed)	Nov 2014 to Mar 2015 (Extended)	Jun 2015 to Oct 2015 (Extended)	Dec 2015 to Mar 2016 (Extended)
B_{WEC} skewness	2.25	2.06	2.34	0.94
B_{MAVEN} skewness	2.34	2.04	1.46	2.34
N_{WEC} skewness	2.46	1.39	2.01	1.26
N_{MAVEN} skewness	3.67	2.29	5.80	3.67
P_{WEC} skewness	2.32	2.13	2.58	1.39
P_{MAVEN} skewness	3.96	2.09	10.04	3.96
T_{WEC} skewness	2.39	2.53	4.39	1.33
T_{MAVEN} skewness	1.18	1.46	1.46	1.18
V_{WEC} skewness	0.20	1.10	0.56	0.72
V_{MAVEN} skewness	0.72	1.00	0.94	0.72

Table 2
Skewness and Kurtosis Values of the Five Solar Wind Parameters for WEC and MAVEN

Parameter	Dec 2015 to Mar 2016 (Detailed)	Nov 2014 to Mar 2015 (Extended)	Jun 2015 to Oct 2015 (Extended)	Dec 2015 to Mar 2016 (Extended)
B_{WEC} kurtosis	6.18	6.10	7.26	0.74
B_{MAVEN} kurtosis	8.00	7.53	2.93	8.00
N_{WEC} kurtosis	7.09	2.36	6.56	1.39
N_{MAVEN} kurtosis	23.99	6.39	56.53	23.99
P_{WEC} kurtosis	6.46	6.79	30.99	3.49
P_{MAVEN} kurtosis	26.73	5.16	158.69	26.73
T_{WEC} kurtosis	7.24	10.28	4.39	2.53
T_{MAVEN} kurtosis	1.54	0.16	2.44	1.54
V_{WEC} kurtosis	−0.64	$-8.6 * 10^{-3}$	−0.30	1.10
V_{MAVEN} kurtosis	0.02	0.72	2.02	0.02

Note. The negative values indicated data that are skewed left, and positive values indicated data that are skewed right. Smaller kurtosis values represent data with fewer deviations from the mean.

and variability of the detailed and extended run. Tables 1 and 2 display calculated skewness and kurtosis values for the detailed simulation as well as the extended simulation compared to MAVEN. Regarding Table 1, skewness provides information on how outlier events impact the shape of the distribution. Skewness is a measure of symmetry or the lack thereof. Keeping this in mind, the skewness for a normal distribution is zero. We can therefore look to the calculated values from both MAVEN and the model for the five solar wind parameters to see if the model's skewness is commensurate. For the detailed run all parameters are skewed right as are the MAVEN parameters. Magnetic field magnitude has a right skew (2.25) closest to MAVEN's magnetic field magnitude skew (2.34) suggesting that the run captured the distribution around the mean best out of the other parameters. The first winter period of the extended run was successful in capturing the skewness of MAVEN's recorded *B* field magnitude, dynamic pressure, and radial velocity. For the summer season, the model did not capture the skewness of the MAVEN data set as well predominantly in dynamic pressure. For the second winter season, which overlaps in time with the detailed run, the model had an identical skewness score to MAVEN for radial velocity.

Table 2 contains the kurtosis values for each parameter. The kurtosis of a data set is defined as the standardized fourth population moment about the mean (Kim, 2013). It is a measure of outlier event impacts on a data set relative to a normal distribution. A higher kurtosis value is produced by infrequent extreme deviations from the mean, as is expected for times of CME impact. The detailed simulation found a kurtosis of −0.64 for radial velocity, indicating that the distribution produced fewer and less extreme outliers than a normal distribution. This was also true for the extended simulation's first winter and summer season, with kurtosis values of −8.6E-3 and −0.30 respectively. In both simulations, the model exhibits frequent smaller deviations from the mean as is evident by the smaller-valued kurtosis measurements relative to MAVEN.

To measure prediction accuracy of the two models, we also calculated the mean-square error (MSE). Averaging the three season's MSEs during the extended time period, it was found that the average MSE for IMF strength was 11.79 nT^2 and 10.11 nT^2 for the detailed run. The proton density (*N*) had a MSE of 11.50 cm^{-6} for the extended and 8.70 cm^{-6} for the detailed. The dynamic pressure (*P*) was 0.74 nPa^2 for the extended and 0.72 nPa^2 for the detailed. Proton temperature (*T*) MSE was calculated to be 50.79 eV^2 for the extended and

Table 3
Mean Square Error Between WSA-ENLIL+Cone Model Results and MAVEN Observations for the Extended and Detailed Time Periods

Time Period	MSE *B* (nT^2)	MSE *N* (cm^{-6})	MSE *P* (nPa^2)	MSE *T* (eV^2)	MSE *V* (km^2/s^2)
Dec 2015 to Mar 2016 (detailed)	10.11	8.70	0.72	44.83	1.21×10^4
Dec 2015 to Mar 2016 (extended)	7.80	8.00	0.72	43.85	1.07×10^4
Jun 2015 to Oct 2015 (extended)	10.03	11.96	0.88	50.88	1.23×10^4
Nov 2014 to Mar 2015 (extended)	17.53	14.55	0.62	57.66	1.59×10^4

Table 4
Ratio of Medians Between the WSA-ENLIL+Cone Model Results and Maven Observation for Each Time Period

Time Period	B_{WEC} / B_{MAVEN}	N_{WEC} / N_{MAVEN}	P_{WEC} / P_{MAVEN}	T_{WEC} / T_{MAVEN}	V_{WEC} / V_{MAVEN}
Dec 2015 to Mar 2016 (detailed)	0.39	0.56	0.54	0.31	1.01
Dec 2015 to Mar 2016 (extended)	0.69	0.62	0.73	0.46	1.07
Jun 2015 to Oct 2015 (extended)	0.54	0.68	0.71	0.33	1.03
Nov 2014 to Mar 2015 (extended)	0.55	0.60	0.82	0.54	1.17

Note. A value of 0 displays better agreement between the two data sets for MSE while values closer to 1 display better agreement between medians.

44.83 eV^2 for the detailed run. Finally, radial solar wind velocity (V) MSE was found to be 1.3E4 km^2/s^2 for the extended run compared to 1.21E4 km^2/s^2 for the detailed. These results are summarized in Table 3. Note that a value closer to zero displays better agreement between the two data sets.

Continuing with the parameter comparisons in Table 4, we found the ratio of median values modeled by WSA-ENLIL+Cone and observed by various MAVEN instruments for the detailed run and for the extended run. Ratios of medians were evaluated because medians have robustness of validity, meaning they are not greatly affected by outliers. Here values closer to 1 display excellent agreement between the model and the observations. We see that the averaged median ratio of the IMF strength estimated by WSA-ENLIL+Cone compared to MAVEN (B_{WEC}/B_{MAVEN}) for the extended run is 0.59 compared to the detailed run that was 0.39. Averaged (N_{WEC}/N_{MAVEN}) for the extended run was 0.63 and 0.56 for the detailed. Averaged (P_{WEC}/P_{MAVEN}) was 0.75 for the extended period compared to 0.54 for the detailed period. (T_{WEC}/T_{MAVEN}) for the extended time period was 0.44 compared to 0.31 for the detailed period. (V_{WEC}/V_{MAVEN}) was 1.09 for the extended period and 1.01 for the detailed period.

Table 5
Comparison of Means Between MAVEN and the WSA-ENLIL+Cone Model Data Set

	SW parameter	Difference of means	Standard error	95% CI	*t* statistic	*P*
Dec 2015 to Mar 2016 (detailed)	*B*	2.02	0.14	1.75–2.29	14.87	<0.0001
	N	1.05	0.15	0.76–1.33	7.16	<0.0001
	P	0.37	0.04	0.28–0.45	8.79	<0.0001
	T	5.04	0.25	4.55–5.53	20.09	<0.0001
	V	7.87	5.65	−3.24–18.97	1.39	0.1646
Nov 2014 to Mar 2015 (extended)	*B*	2.66	0.15	2.37–2.95	18.07	<0.0001
	N	2.37	0.18	2.02–2.72	13.24	<0.0001
	P	0.34	0.04	0.27–0.41	9.51	<0.0001
	T	4.31	0.26	3.7–4.71	16.43	<0.0001
	V	−77.05	5.15	−87.15 to −66.95	14.97	<0.0001
Jun 2015 to Oct 2015(extended)	*B*	1.77	0.10	1.57–1.97	17.37	<.0001
	N	0.97	0.13	0.72–1.22	7.55	<0.0001
	P	0.25	0.04	0.18–0.32	6.84	<0.0001
	T	5.14	0.20	4.76–5.52	26.23	<0.0001
	V	−19.23	4.12	−27.31 to −11.15	4.67	<0.0001
Dec 2015–Mar 2016 (extended)	*B*	1.44	0.13	1.19–1.68	11.50	<0.0001
	N	1.13	0.13	1.06–1.57	10.23	<0.0001
	P	0.36	0.04	0.28–0.43	9.21	<0.0001
	T	4.49	0.24	4.01–4.97	18.51	<0.0001
	V	−21.14	5.29	−31.52 to −10.75	3.99	0.0001

Note. Statistics include standard error, 95% confidence interval of the difference, the *t* statistic, and *P* value of obtaining the observed difference between the data sets.

Table 6
T Statistic and P Value for Fast and Slow Solar Wind Parameters for the Detailed and Extended Run

		SW parameter	*t* statistic	*P* value
Dec 2015 to Mar 2016 (detailed)	Slow solar wind	*N*	-	-
		T	20.92	<0.0001
		V	3.10	0.002
	Fast solar wind	*N*	6.85	<0.0001
		T	-	-
		V	0.84	0.40
Nov 2014 to Mar 2015 (extended)	Slow solar wind	*N*	-	-
		T	16.55	<0.0001
		V	14.31	<0.0001
	Fast solar wind	*N*	13.34	<0.0001
		T	-	-
		V	0.55	0.58
Jun 2015 to Oct 2015 (extended)	Slow solar wind	*N*	-	-
		T	29.09	<0.0001
		V	1.39	0.16
	Fast solar wind	*N*	8.55	<0.0001
		T	-	-
		V	1.28	0.20
Dec 2015 to Mar 2016 (extended)	Slow solar wind	*N*	-	-
		T	19.01	<0.0001
		V	5.16	<0.0001
	Fast solar wind	*N*	11.63	<0.0001
		T	-	-
		V	1.10	0.27

Note. That a dash represents no WEC data existing for that parameter.

To conduct an all-encompassing comparison of means, we then calculated the two-sample *t* test as described in Snedecor and Cochran (1996). Briefly stating the importance of the *t* test, the computation calculates the difference between the observed means in two independent data sets. The summary statistics returned from the test include the difference of the means, the standard error between the means, a 95% confidence interval (CI), the *t* statistic, and a significance value commonly referred to as the *P* value. The *P* value is defined as the probability of obtaining the observed differences between data sets if the difference between the two means was zero (otherwise known as the null hypothesis). If the *P* value is low ($P < 0.05$), the variances of the two samples cannot be assumed to be equal. The *t* statistic measures the size of the difference relative to the variation of the data sets. Larger *t* statistics represent evidence that there is significant difference from the two data sets. Table 5 lists the summary of statistics. It was found that for the detailed simulation, the only solar wind parameter that was above the conventional 0.05 *P* value was that of the radial velocities, reaching a *P* value of 0.16. The extended simulation did not reach *P* values higher than 0.0001, causing the null hypothesis to be rejected. We therefore conclude that the WSA-ENLIL+Cone model's and MAVEN's means for each of the five solar wind parameters differed considerably.

Delving a little deeper into calculating *t* test statistics and taking into consideration that solar wind exists in two fundamental states of slow and fast, we sorted each data set into corresponding fast and slow solar wind. Based off of Schwenn (2001) definitions of average solar wind parameters for times around solar minimum, we classified slow solar wind as having an average radial velocity between 250 and 400 km/s, a proton density of ~ 10.7 cm^{-3}, and proton temperature of ~ 3 eV. Fast solar wind, on the other hand, was classified as having an average velocity between 400 and 800 km/s, an average proton density of ~ 3 cm^{-3}, and proton temperature averaging ~ 19.82 eV. Based on these definitions of fast and slow solar wind, once more we calculated the

two-sample *t* test for the unpaired data sets. For the sake of brevity, we have only included the absolute value of the *t* statistic and the significance level (*P* value). Table 6 includes the *t* statistic and its *P* value for proton density, proton temperature, and radial velocity for fast and slow solar wind. While categorizing slow and fast solar wind, there were instances where the WSA-ENLIL+Cone model's orbit-averaged data did not include any values matching Schwenn (2001) averages. These are identified in Table 6 as dash marks. It was found that for the detailed run, fast solar wind radial velocity had the highest *P* value, reaching 0.40. For the extended run, fast solar wind radial velocity again had the highest *P* values. These *P* values, in chronological order, were 0.58, 0.20, and 0.27. For the summer season of the extended run, the slow solar wind velocity had a *P* value of 0.16, exhibiting statistical significance.

4. Discussion and Conclusion

The data provided by spacecraft orbiting Mars allow model developers to regularly adjust solar wind and interplanetary magnetic field modeling for reliability and overall validity. It has been shown in multiple studies (e.g., Dewey et al., 2015, 2016; Lee et al., 2015) that even in detailed runs, the WSA-ENLIL+Cone model does not completely capture trends of observed solar wind and IMF properties (e.g., underprediction of IMF strength, systematic over prediction of temperature). There is still much work to be done, such as using in situ observations from multiple spacecraft to cross-check model outcomes.

Regarding the inaccuracies of amplitudes and arrival times of CME shocks, we can turn to the mathematical description of ENLIL to see what postulations are made. In Odstrčil (2003) a magnetohydrodynamic (MHD) approximation was used. Included in the approximation are equations for total mass density, mean flow velocity, magnetic field, total pressure, and thermal energy. It is noted that in this MHD approximation, thermal energy is used instead of total energy to produce smooth profiles for the thermal pressure and temperature. With the use of this thermal energy equation, it is recognized that it may lead to inaccuracies in speed and amplitude of strong shocks. The discrepancies in CME arrival times can also be attributed to the inverse correlation between solar wind speed and density (see Lee et al., 2013). The spherical plasma clouds used in simulation are initialized to have uniform velocities along with temperatures being set equal to that of the ambient fast solar winds. The ratio of the CME cloud density to the ambient fast solar wind density is not discernible from observations, therefore the plasma cloud, by default, has a larger dynamic pressure value than the pressure of the ambient fast wind. This results in the modeled CME being injected into a denser solar wind stream that is moving at relatively slow speeds. This causes the CME shock arrival time to be later than observed, as proven by Taktakishvili et al. (2010).

High-speed stream arrival times can be impacted by WSA coronal maps that contain small latitudinal shifts in the magnetogram-derived coronal maps. These shifts, as pointed out in Mays et al. (2015), can be caused by inaccuracies in solar magnetic field observations subsequently causing large longitudinal shifts in the solar wind structure. With improvements to global photospheric maps using magnetic flux transport models or the implementation of intercalibrated magnetograms from multiple sources, we would be able to predict the magnetic field in locations where direct measurements are not available or possible. This would in turn improve background solar wind modeling, subsequently improving CME event densities.

Turning to the Cone model, there exists variations in cone parameters generated for each CME event. Due to the fact that the cone model relies on manual fits of an ellipse over a white light coronagraph of a CME, ambiguities in identifying the ejecta structure lead to discord in 3-D CME kinematic and geometric parameter estimations. Furthermore, there are known assumptions of CME properties such as isotropic expansion of CMEs, radial propagation, and constant CME cone angular width. Also due to temporal and spatial resolution limitations, the model is constructed to only reproduce large-scale magnetic configurations. This translates to the model not incorporating magnetic fields within ejecta such as flux ropes. As found by Falkenberg et al. (2011), many ICMEs change direction in propagation, so assuming radial propagation from their point of origin may not be valid in all cases. Zhao et al. (2002) in turn concludes that numerous CMEs propagate almost radially, signifying that their angular widths remain nearly constant throughout the corona and therefore provide a basis for propagation.

Both the extended and detailed run discrepancies with in situ observations are inherently linked to these various assumptions in each model. It can be asserted that the WSA-ENLIL+Cone model could one day provide a point of reference for solar wind parameters such as radial velocity for extensive and/or short time periods. We have shown this through collating multiple statistics such as skewness and kurtosis measurements,

the two-sample *t* tests for five important solar wind parameters, comparison of fast and slow solar wind data, MSE values, and ratios of medians. Conducting systematic validation of the model in both solar minima and maxima can highlight the underlying problems experienced when forecasting solar wind parameters to planetary orbital locations. This study was an effort to contribute to the model's development and to establish that generalized simulations, which include less solar transient events, perform the same as comprehensive runs.

We, therefore, conclude that with current-day restrictions of computational-grid resolutions among other things, the long-term simulations demonstrate no loss of detail compared to shorter, exhaustive simulations. Generally, solar wind modeling should be used in conjunction with other techniques such as solar wind proxies to provide more thorough characterizations of solar wind conditions at Mars. As low computational overhead becomes less of a worry, each new refinement of the model will be expected to render more realistic computations. In this case, long-term forecasts might continue to have imprecise predictions; however, the short all-inclusive forecasts will be closer to what is actually observed in nature.

Acknowledgments
The MAVEN project is supported by NASA through the Mars Exploration Program. All original MAVEN data reported in this paper are archived by the NASA Planetary Data System (https://pds.nasa.gov/) and are available for public use. C. L. Lentz thanks M. L. Mays for providing valuable input on the models and who also conducted all of the simulations. The modeling techniques described in this paper were originally developed under the auspices of the National Science Foundation's Center for Integrated Space Weather Modeling (CISM). Simulation results have been provided by the Community Coordinated Modeling Center at the Goddard Space Flight Center through their public Runs on Request system (ccmc.gsfc.nasa.gov; run numbers: Christy_Lentz_081216_SH_1, Christy_Lentz_081216_SH_2, Christy_Lentz_081216_SH_3, Christy_Lentz_081216_SH_4, Christy _Lentz_081216_SH_5, and Christy_Lentz_01102017_SH_1). The WSA model was developed by N. Arge (NASA GSFC), and the ENLIL model was developed by D. Odstrčil (GMU).

References

Acuña, M. H., Connerney, J. E. P., Wasilewski, P., Lin, R. P., Anderson, K. A., Carlson, C. W., … Ness, N. F. (1992). Mars observer magnetic fields investigation. *Journal of Geophysical Research*, *97*(E5), 7799–7814. https://doi.org/10.1029/92JE00344

Acuña, M. H., Connerney, J. E. P., Wasilewski, P., Lin, R. P., Anderson, K. A., Carlson, C. W., … Ness, N. F. (1998). Magnetic field and plasma observations at Mars: Initial results of the Mars Global Surveyor mission. *Science*, *279*(5357), 1676–1680. https://doi.org/10.1126/science.279.5357.1676

Arge, C. N., & Pizzo, V. J. (2000). Improvement in the prediction of solar wind conditions using near-real time solar magnetic field updates. *Journal of Geophysical Research*, *105*(A5), 10,465–10,479. https://doi.org/10.1029/1999JA000262

Arge, C. N., Luhmann, J. G., Odstrčil, D., Schrijver, C. J., & Li, Y. (2004). Stream structure and coronal sources of the solar wind during the May 12th, 1997 CME. *Journal of Atmospheric and Solar-Terrestrial Physics*, *66*, 1295–1309. https://doi.org/10.1016/j.jastp.2004.03.018

Baker, D. N., Odstrčil, D., Anderson, B. J., Arge, C. N., Benna, M., Gloeckler, G., … Zurbuchen, T. H. (2009). Space environment of mercury at the time of the first MESSENGER flyby: Solar wind and interplanetary magnetic field modeling of upstream conditions. *Journal of Geophysical Research*, *114*, A10101. https://doi.org/10.1029/2009JA014287

Baker, D. N., Odstrčil, D., Anderson, B. J., Arge, C. N., Benna, M., Gloeckler, G., & Zurbuchen, T. H. (2011). The space environment of Mercury at the times of the second and third MESSENGER flybys. *Planetary and Space Science*, *59*(15), 2066–2074. https://doi.org/10.1016/j.pss.2011.01.018

Baker, D. N., Poh, G., Odstrčil, D., Arge, C. N., Benna, M., Johnson, C. L., … Zurbuchen, T. H. (2013). Solar wind forcing at Mercury: WSA-ENLIL model results. *Journal of Geophysical Research: Space Physics*, *118*, 45–57. https://doi.org/10.1029/2012JA018064

Barabash, S., Lundin, R., Andersson, H., Brinkfeldt, K., Grigoriev, A., Gunell, H., … Wurz, P. (2006). The Analyzer of Space Plasmas and Energetic Atoms (ASPERA-3) for the Mars Express mission. *Space Science Reviews*, *126*, 113–164. https://doi.org/10.1007/s11214-006-9124-8

Connerney, J. E. P., Espley, J., Lawton, P., Murphy, S., Odom, J., Oliverson, R., & Sheppard, D. (2015). The MAVEN magnetic field investigation. *Space Science Reviews*, *195*, 257–291. https://doi.org/10.1007/s11214-015-0169-4

Dewey, R. M., Baker, D. N., Anderson, B. J., Benna, M., Johnson, C. L., & Korth, H. (2015). Improving solar wind modeling at Mercury: Incorporating transient solar phenomena into the WSA-ENLIL model with the CONE extension. *Journal of Geophysical Research: Space Physics*, *120*, 5667–5685. https://doi.org/10.1002/2015JA021194

Dewey, R. M., Baker, D. N., Mays, M. L., Brain, D. A., Jakosky, B. M., Halekas, J. S., … Lee, C. O. (2016). Continuous solar wind forcing knowledge: Providing continuous conditions at Mars with the WSA-ENLIL+Cone model. *Journal of Geophysical Research: Space Physics*, *121*, 6207–6222. https://doi.org/10.1002/2015JA021941

Domingo, V., Fleck, B., & Poland, A. I. (1995). SOHO: The Solar and Heliospheric Observatory. *Space Science Reviews*, *1–2*, 81–84. https://doi.org/10.1007/BF00768758

Edberg, N. J. T., Brain, D. A., Lester, M., Cowley, S. W. H., Modolo, R., Fränz, M., … Barabash, S. (2009). Plasma boundary variability at Mars as observed by Mars Global Surveyor and Mars Express. *Annales Geophysicae*, *27*(9), 3537–550. https://doi.org/10.5194/angeo-27-3537-2009

Falkenberg, T. V., Taktakishvili, A., Pulkkinen, A., Vennerstrom, S., Odstrčil, D., Brain, D. A., … Mitchell, D. (2011). Evaluating predictions of ICME arrival at Earth and Mars. *Space Weather*, *9*, S00E12. https://doi.org/10.1029/2011SW000682

Halekas, J. S., Taylor, E. R., Dalton, G., Johnson, G., Curtis, D. W., McFadden, J. P., … Jakosky, B. M. (2015). The solar wind ion analyzer for MAVEN. *Space Science Reviews*, *195*, 125–151. https://doi.org/10.1007/s11214-013-0029-z

Harvey, J. W., Hill, F., Hubbard, R. P., Kennedy, J. R., Leibacher, J. W., Pintar, J. A., … Yasukawa, E. (1996). The Global Oscillation Network Group (GONG) project. *Science*, *272*(5266), 1284–1286. https://doi.org/10.1126/science.272.5266.1284

Howard, R. A., Moses, J. D., Vourlidas, A., Newmark, J. S., Socker, D. G., Plunkett, S. P., … Carter, T. (2008). Sun Earth Connection Coronal and Heliospheric Investigation (SECCHI). *Space Science Reviews*, *136*(1–4), 67–115. https://doi.org/10.1007/s11214-008-9341-4

Jakosky, B. M., Grebowsky, J. M., Luhmann, J. G., Connerney, J. E. P., Eparvier, F., Ergun, R., … Yelle, R. (2015). MAVEN observations of the response of Mars to an interplanetary coronal mass ejection. *Science*, *350*(6261). https://doi.org/10.1126/science.aad0210

Kaiser, M. L., Kucera, T. A., Davila, J. M., St. Cyr, O. C., Guhathakurta, M., & Christian, E. (2007). The STEREO mission: An introduction. *Space Science Reviews*, *136*(1–4), 5–16. https://doi.org/10.1007/s11214-007-9277-0

Kim, H. Y. (2013). Statistical notes for clinical researchers: Assessing normal distribution (2) using skewness and kurtosis. *Restorative Dentistry and Endodontics*, *38*(1), 52–54. https://doi.org/10.5395/rde.2013.38.1.52

Larson, D. E., Lillis, R. J., Lee, C. O., Dunn, P. A., Hatch, K., Robinson, M., … Jakosky, B. M. (2015). The MAVEN solar energetic particle investigation. *Space Science Reviews*, *195*(1–4), 153–172. https://doi.org/10.1007/s11214-015-0218-z

Lee, C. O., Arge, C. N., Odstrčil, D., Millward, G., Pizzo, V., Quinn, J. M., & Henney, C. J. (2013). Ensemble modeling of CME propagation. *Solar Physics*, *285*(1–2), 349–368. https://doi.org/10.1007/s11207-012-9980-1

Lee, C. O., Arge, C. N., Odstrčil, D., Millward, G., Pizzo, V., & Lugaz, N. (2015). Ensemble modeling of successive halo CMEs: A case study. *Solar Physics*, *290*, 1207–1229. https://doi.org/10.1007/s11207-015-0667-2

Lee, C. O., Hara, T., Halekas, J. S., Thiemann, E., Chamberlin, P., Eparvier, F., … Jakosky, B. M. (2017). MAVEN observations of the solar cycle 24 space weather conditions at Mars. *Journal of Geophysical Research: Space Physics*, *122*, 2768–2794. https://doi.org/10.1002/2016JA023495

Mays, M. L., Taktakishvili, A., Pulkkinen, A., MacNeice, P. J., Rastätter, L., Odstrčil, D., … Kuznetsova, M. M. (2015). Ensemble modeling of CMEs using the WSA-ENLIL cone model. *Solar Physics*, *290*(6), 1775–1814. https://doi.org/10.1007/s11207-015-0692-1

Millward, G., Biesecker, D., Pizzo, V., & De Koning, C. A. (2013). An operational software tool for the analysis of coronagraph images: Determining CME parameters for input into the WSA-ENLIL heliospheric model. *Space Weather*, *11*(2), 57–68. https://doi.org/10.1002/swe.20024

Mitchell, D. L., Mazelle, C., Sauvaud, J. A., Thocaven, J., Rouzaud, J., Fedorov, A., … Jakosky, B. M. (2016). The MAVEN solar wind electron analyzer. *Space Science Reviews*, *200*, 495–528. https://doi.org/10.1007/s11214-015-0232-1

Odstrčil, D. (2003). Modeling 3-D solar wind structure. *Advances in Space Research*, *32*(4), 497–506. https://doi.org/10.1016/S0273-1177(03)00332-6

Odstrčil, D., Linker, J. A., Lionello, R., Mikic, Z., Riley, P., Pizzo, V. J., & Luhmann, J. G. (2002). Merging of coronal and heliospheric numerical two-dimensional MHD models. *Journal of Geophysical Research*, *107*(A12), 1493. https://doi.org/10.1029/2002JA009334

Schatten, K. H., Wilcox, J. M., & Ness, N. F. (1969). A model of interplanetary and coronal magnetic fields. *Solar Physics*, *6*, 442–455. https://doi.org/10.1007/BF00146478

Schwenn, R. (2001). *Solar wind: Global properties, Encyclopedia of Astronomy and Astrophysics* (2301 pp.). Bristol: Institute of Physics. https://doi.org/10.1888/0333750888/2301

Sheeley Jr., N. R. (2017). Origin of the Wang-Sheeley-Arge solar wind model. *History of Geophysics and Space Sciences*, *8*, 21–28. https://doi.org/10.5194/hgss-8-21-2017

Snedecor, G. W., & Cochran, W. G. (1996). *Statistical methods* (Vol. 8). Ames, IA: Iowa State University Press.

Taktakishvili, A., Kuznetsova, M., MacNeice, P., Hesse, M., Rastätter, L., & Pulkkinen, A. (2009). Validation of the coronal mass ejection predictions at the Earth orbit estimated by ENLIL heliosphere cone model. *Space Weather*, *7*, S03004. https://doi.org/10.1029/2008SW000448

Taktakishvili, A., MacNeice, P., & Odstrcil, D. (2010). Model uncertainties in predictions of arrival of coronal mass ejections at Earth orbit. *Space Weather*, *8*, S06007. https://doi.org/10.1029/2009SW000543

Wang, Y. M., & Sheeley, N. R. (1992). On potential field models of the solar corona. *Astrophysical Journal*, *392*, 310–319. https://doi.org/10.1086/171430 Xie

Xie, H., Ofman, L., & Lawrence, G. (2004). Cone model for halo CMEs: Application to space weather forecasting. *Journal of Geophysical Research*, *109*, A03109. https://doi.org/10.1029/2003JA010226

Zender, J., Delhaise, F., Arviset, C., Heather, D., Diaz Del Rio, J., Manaud, N., … Slavney, S. (2009). Mars Express: The scientific investigations.

Zhao, X. P., Plunkett, S. P., & Liu, W. (2002). Determination of geometrical and kinematical properties of halo coronal mass ejections using the cone model. *Journal of Geophysical Research*, *107*(A8), 1223. https://doi.org/10.1029/2001JA009143